Demonstration of Optical Clock-Free Localization and Navigation (CLAN)

Mustafa Mert Bayer, Ataberk Atalar, Xun Li, Haoyu Xie, and Ozdal Boyraz, *Member, IEEE*

***Abstract*—Positioning, navigation, and timing (PNT) applications often rely on establishing synchronized clocks to achieve accurate localizations. The accuracy of the measurement is compromised due to clock drifts or inaccurate timing. In this manuscript, we propose and demonstrate autonomous optical clock-free localization and navigation (CLAN) system that eliminates the need for synchronized clocks and uses free-running lasers at the transmitter and receiver sites. Experimentally we show that a remote static or dynamic receiver >1.8 km away from the transmitter determines its relative location to the transmitter with a <1 cm uncertainty and successfully identifies >2 cm incremental changes in distance without using time information. The experimental results are also verified by theoretical modeling and numerical simulations. The proposed technology is proven to be suitable for long-range localizations, autonomous navigations, and timing distributions in GPS-denied environments.**

***Index Terms*—Lidar, microwave photonics, photonic localization, photonic navigation.**

I. Introduction

OVER the years, global positioning systems (GPS), and positioning, navigation, and timing (PNT) applications have become a vital part of daily life [1]. Traditional radio frequency (RF) based PNT architectures [2], [3] are dominating the industry by providing services to numerous areas of applications, including transportation [4], autonomous vehicles [5], geophysical exploration [6], indoor navigation [7], precision agriculture [8], and defense applications [9], [10]. GPS works by triangulating the user's position based on the time it takes to transmit signals from the satellites to the user's GPS receiver (Rx) [11]. Each satellite transmits a unique code at a precise time, and the Rx uses this information to calculate its distance from the satellite [12]. By measuring the distances from a minimum of four satellites, the Rx can triangulate its exact location in three-dimensional space [13]. As is clear, the heart of the satellite-based GPS is the atomic reference clock that generates a fundamental frequency of 10.23 MHz, and satellites transmit signals in the integer multiples of the employed clock [14]. Alternatively, navigation by the signal of opportunities that utilize existing RF radiation in the environment has been investigated heavily to provide PNT in GPS-denied environments [15], [16], [17], [18], [19].

Nowadays, optical chip-scale GPS and PNT systems are emerging as a new approach for positioning [20], navigation, and timing by using optical carriers [21] instead of the traditional radio frequency (RF) signals. These systems have the potential to provide more accurate, secure, and reliable location information in a variety of environments, including indoors [22], [23], [24], and in urban canyons [25], [26] where radio frequency signals may be obstructed. Similarly, various autonomous optical navigation methods were investigated for space missions for landing and localization purposes [27], [28], [29]. Up to date, the optical navigation techniques relying on CCD cameras [30], [31], frequency combs [32], and ultra-narrow linewidth lasers [33], [34] were evaluated to achieve photonics-based localization. As in RF-based methods, most optical PNT techniques rely on synchronized atomic clocks [35].

In this article, we introduce an alternative optical clock-free localization and navigation (CLAN), which eliminates the need for any time synchronization between the optical transmitter (Tx) and an Rx. Additionally, the proposed CLAN utilizes free-running lasers as an optical source at Tx and local oscillators at Rx without using a clock recovery circuit or photonic frequency locking. To prove the concept, we present the experimental demonstration of static or dynamic target localization at a 1.8 km distance with less than 1 cm uncertainty. We also show that the optical CLAN technique can resolve a 2 cm incremental change of target locations after a 1.8 km optical path length. The proposed method utilizes an amplitude-modulated continuous-wave (CW) laser by the combination of multiple RF tones at the Tx side and a free-running local oscillator CW laser at the Rx side for heterodyne detection. The RF tones are selected to be harmonics of a common reference oscillator and are phase-locked to each other at the Tx. Localization algorithms [36], [37] utilize the phases of intermediate frequency (IF) tones generated by the cross-beatings of the detected RF tones to eliminate random phase noise and decoherence between the Tx lasers and the free-running local oscillator.

Foremost, the proposed signal processing technique, which can be performed in the digital or analog domain, eliminates the common phase noise of lasers and hence provides ultra-long-range localization capability to the proposed CLAN technique regardless of the coherence length of lasers, as well as

Manuscript received 30 December 2022; revised 20 May 2023; accepted 15 June 2023. Date of publication 22 June 2023; date of current version 16 October 2023. This work was supported by the Office of Naval Research under Grant N00014-22-1-2423-P00001. *(Corresponding author: Mustafa Mert Bayer.)*

This work did not involve human subjects or animals in its research.

The authors are with the Electrical Engineering and Computer Science Department, University of California, Irvine, CA 92697 USA (e-mail: bayerm@uci.edu; aatalar@uci.edu; xunl12@uci.edu; xieh10@uci.edu; oboyraz@uci.edu).

Color versions of one or more figures in this article are available at https://doi.org/10.1109/JLT.2023.3288555.

Digital Object Identifier 10.1109/JLT.2023.3288555

the necessity of synchronized clocks. The existing localization techniques are clock-based ranging methods. In general, the range is measured based on the propagation time of the signal. If one can measure the propagation time, as the speed of light is constant, the distance is measured from the propagation time [38]. Similar techniques have been used for many ground-based applications, such as cooperative localization and navigation, as well [9]. Although they offer numerous benefits, they differ from CLAN as they require clocks at the transmitter and receiver or bidirectional signal exchange for time verification. The proposed CLAN technique does not use any time information at all for distance measurement. Localization is performed according to the relative phase variations on the RF sidebands. Moreover, bidirectional signal exchange between the transmitter and receiver is also not required. Therefore, the CLAN technique paves the way for clock-free high-resolution localization and navigation for applications that require cm-level precision in positioning without the time information. The technique can be an ideal solution for the localization and navigation of drones, unmanned or manned aerial vehicles (UAVs), rovers for space missions, inter-satellite navigation for CubeSats, indoor navigation, etc. Lastly, it is important to state that the experimental study showcased herein employs optical carriers, which offer enhanced directionality and security. However, it is worth noting that the CLAN system is equally capable of functioning with RF carriers.

This article's organization is as follows. First, we introduce the concept and present the theoretical model of optical clock-free navigation and localization. Then, we show the numerical simulation results to demonstrate the triangulation algorithm. Finally, we present the experimental setup and the results of the proof-of-concept experiments for static and dynamic targets at an optical path length of ∼1.8 km.

II. Concept

Fig. 1 illustrates the concept of the proposed CLAN technique, where Tx is represented by the ground station, and the target Rx is depicted as a flying drone unit. The CLAN methodology is inspired by the previously developed phase-based multi-tone continuous-wave lidar [36], [37], [39], [40] that can perform ranging and velocimetry measurements at distances far beyond the coherence length of lasers. However, in the CLAN technique, a remote user can measure its relative distance to a Tx terminal from relative phase transformations and navigate by using a constant broadcast of the signal from a known transmitter through a coherent detection system the CLAN uses. Additionally, it is shown that the proposed approach can be realized because the implemented signal processing algorithms can eliminate the decoherence between the local oscillator at the receiver and the carrier oscillator at Tx. Hence, the need for an optical PLL to fix the phase and frequency of the laser at the receiver is eliminated. In this illustration, a CW laser is modulated with three frequencies of f_1, f_2, and f_3 to generate stable RF sidebands. The collimators (CL) at the Rx and Tx represent the transmitter and receiver antennas. The multi-tone modulated laser beam propagates a distance of ΔL to the Rx antenna. The heterodyne

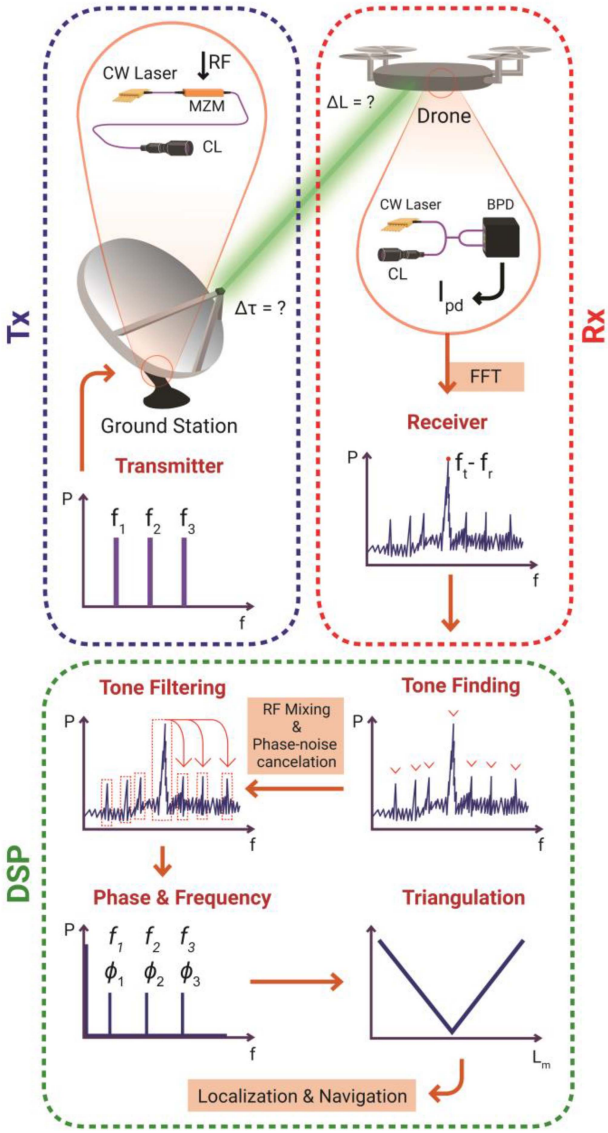

Fig. 1. Illustration of the CLAN concept, where the transmitter is located at the ground station and receiver architecture is embedded into a drone unit on flight. The spectrum indicates the stable phase-locked RF sidebands for three frequencies (f_1, f_2, and f_3) on the transmitter side, where f_t and f_r are the Tx and Rx carrier frequencies, respectively. The digital signal processing (DSP) flow on the receiver side is given for three static RF tones to perform localization via triangulation algorithms.

detection system mixes the received signal with a free-running local CW laser before a balanced photodetector (BPD). It should be noted that the Tx and Rx lasers need to operate at similar frequencies so that the frequency difference is less than the detection bandwidth to capture the sidebands. To satisfy this, the operating temperatures of the lasers are controlled in the proof-of-concept experiments. Utilizing existing technologies such as a pair of frequency-locked ITU-grid telecom lasers operating at similar frequencies removes the necessity for such temperature monitoring.

A Fast Fourier Transform (FFT) is performed on the resulting photocurrent to obtain the corresponding spectrum. In the spectrum, the expected frequency with the maximum peak power is

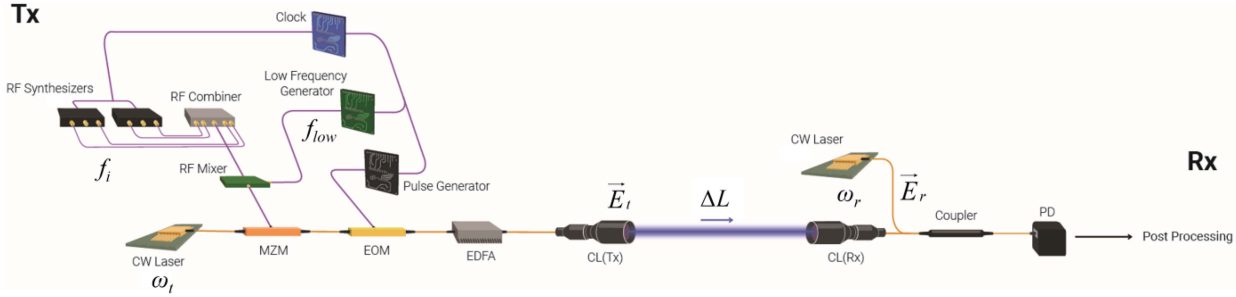

Fig. 2. Schematic of the CLAN architecture to demonstrate the working principle by indicating the corresponding electric fields, and optical and electrical frequencies for Tx and Rx.

attributed to the frequency difference between the Tx and Rx sources, which is indicated as f_t - f_r, where f_t and f_r denote the center frequency of the optical carrier of the Tx and the Rx, respectively. Since the modulation frequencies are predefined, it is possible to locate the frequency-shifted RF sidebands in the spectrum by referencing the maximum frequency peak. After tone localization, bandpass filtering is performed for each tone, including the frequency of f_t - f_r. All resultant phase noise elements due to Tx and Rx lasers are present in the filtered frequencies, including the modulation tones. The filtered frequency of f_t - f_r is further RF mixed with the shifted sidebands with the purpose of not only down-shifting the spectrum back to the baseband but also clearing all the common noise terms over the sidebands. In this configuration, the phase-noise-free f_1, f_2, and f_3 frequencies accumulate phases proportional to L_m and their corresponding frequencies as ϕ_1, ϕ_2, and ϕ_3, respectively. By utilizing the phase information embedded into multiple frequencies, it is possible to triangulate the relative position of the target Rx with respect to the Tx.

III. Theoretical Model

The experimental model used to present the theory of CLAN is shown in Fig. 2. On the transmitter side, a CW laser operating at a frequency of $\omega_t = 2\pi f_t$ is modulated via an MZM that is biased at the quadrature voltage. A total of N phase-locked RF frequencies (f_i) are synthesized and fed to the input port of the MZM after an RF combiner. The modulation yields sidebands stationed near the optical carrier frequency at the selected frequencies of $\omega_t \pm \omega_i$, where $\omega_i = 2\pi f_i$. Since the phase has a 2π cyclic nature, we employ a sub-carrier modulation technique by adding another low-frequency phase-locked low-frequency signal in the kHz range on RF tones. Here, the low-frequency term, $\omega_{low} = 2\pi f_{low}$, is RF mixed with one or multiple high-frequency modulations to have a longer unambiguous range and perform localization with higher accuracy and resolution. For instance, the first modulation frequency after RF mixing with ω_{low} generates tones at $\omega_t \pm \omega_1 \pm \omega_{low}$. Therefore, the time window in the Rx should be selected accordingly to resolve the f_{low}. The modulated signal is further pulsated by an additional electro-optic modulator (EOM) with a high extinction ratio to realize higher peak powers in a quasi-CW configuration.

Then, the multi-frequency modulated signal is amplified via an Erbium-doped fiber amplifier (EDFA) and transferred to the free space via a CL. The electric field equation of the propagating beam after a time-of-flight of $\tau = \Delta L / c$ is given in(1), where c is the speed of light. Here, A_t is the field amplitude of the transmitted light, m is the modulation index, α_t is the linear attenuation realized on the beam path, ϕ_i^{RF}, ϕ_0^t, and $\phi_n^t(t-\tau)$ are the initial RF phase, initial carrier phase, and the Tx laser phase noise after, respectively. The CL of the Rx side collects the transmitted light after propagating a distance ΔL with the speed of light *c/n,* where is the refractive index of the propagation medium.

$$E_t = \frac{A_t}{\sqrt{2}}\alpha_t \exp\left[j\omega_t t + j\phi_0^t + j\omega_t \frac{\Delta L}{c} + j\phi_n^t(t-\tau)\right] - \frac{mA_t}{4\sqrt{2}}\alpha_t \sum_{i=1}^{N}\left(\begin{array}{l}\exp\left[\begin{array}{l}j(\omega_t+\omega_i)t + j\phi_0^t + j\phi_i^{RF} \\ +j(\omega_t+\omega_i)\frac{\Delta L}{c} + j\phi_n^t(t-\tau)\end{array}\right] \\ +\exp\left[\begin{array}{l}j(\omega_t-\omega_i)t + j\phi_0^t - j\phi_i^{RF} \\ +j(\omega_t-\omega_i)\frac{\Delta L}{c} - j\phi_n^t(t-\tau)\end{array}\right]\end{array}\right) \quad (1)$$

Then the beam is combined with the laser on the receiver side with a local oscillator frequency of ω_r to strengthen the collected modulation tones through an optical heterodyne detection so that the detection scheme is shot noise limited. The electric field of the local oscillator laser in the receiver can be formalized as in (2), where A_r, ϕ_0^r and $\phi_n^r(t)$ are the amplitude, initial phase of the CW laser, and the laser phase noise, respectively.

$$E_r = A_r \exp(j\omega_r t + j\phi_0^r + j\phi_n^r(t)) \quad (2)$$

the local oscillator is a free-running laser without any frequency and phase locking to the remote transmitter. The only constraint, as mentioned earlier, is the maintaining frequency difference within the detector bandwidth, which can be easily achieved by using standard telecom lasers. Hence, time synchronization is not necessary to position the Rx. The resultant beam is transmitted to the photodetector (PD) with a responsivity of R to generate the photocurrent (I_{pd}) as given in (3), where I_{DC} is the DC portion of the photocurrent, and the self-beating terms are neglected for simplicity. The amplitudes are $A' = 2RA_tA_r\alpha_t/\sqrt{2}$ and $A'' = mRA_tA_r\alpha_t/2\sqrt{2}$. Also, the initial phase difference

between the Tx and Rx lasers is defined as $\Phi = \phi_0^t - \phi_0^r$.

$$I_{pd} = I_{DC} + A' \cos\Big((\omega_t - \omega_r)\, t + \omega_t \frac{\Delta L}{c} + \Phi + \phi_n^t(t-\tau) - \phi_n^r(t) \Big) - A'' \left[\begin{matrix} \sum_{i=1}^{N} \cos \begin{pmatrix} (\omega_t - \omega_r + \omega_i)\, t + (\omega_t + \omega_i)\, \frac{\Delta L}{c} \\ +\Phi + \phi_i^{RF} + \phi_n^t(t-\tau) - \phi_n^r(t) \end{pmatrix} \\ + \sum_{i=1}^{N} \cos \begin{pmatrix} (\omega_t - \omega_r - \omega_i)\, t - (\omega_t - \omega_i)\, \frac{\Delta L}{c} \\ +\Phi - \phi_i^{RF} - \phi_n^t(t-\tau) - \phi_n^r(t) \end{pmatrix} \end{matrix} \right] \tag{3}$$

In the resultant spectrum, the highest peak power will be realized at f_t - f_r, and it is possible to use this peak as a reference to locate the modulation tones by using the apriori knowledge of the preselected tone frequencies. Then, digital bandpass filters near the RF tones can be employed to generate the filtered waveforms of the individual tones, including the peak at f_t - f_r. As can be seen in (3), all frequency components, including the sidebands possess the same phase noise and Φ due to Tx and Rx lasers. To cancel the common noise terms and shift the spectrum back to the baseband, the filtered f_t - f_r signal is RF mixed with the I_{pd} spectrum. The intermediate frequency (IF) term of the RF sidebands is given in (4), where A_{IF} represents the amplitude of the IF signal. After RF mixing, the common noise terms are canceled, and the remaining ϕ_i^{RF} can be eliminated with pre-calibration of the phases of the RF tones through RF synthesizers.

$$I_{IF} = A_{IF} \sum_{i=1}^{N} \left[\cos\left(\omega_i t + \omega_i \frac{\Delta L}{c} + \phi_i^{RF} \right) \right] \tag{4}$$

The phase-noise-free filtered sidebands store the information about ΔL in the phase of each modulation tone. By utilizing the relative phase and frequencies of the tones, it is possible to acquire the target displacement. To do so, the refined sidebands in (4) are RF mixed, which yields $A_i A_j \cos(\Delta\omega_{i,j} t \pm \Delta\phi_{i,j})$, where A_i, A_j, $\Delta\phi_{i,j}$, and $\Delta\omega_{i,j}$ are the amplitudes, phase differences, and frequency differences of *i*th and *j*th tones, respectively. As a result, the target location can be estimated using (5), where n is an integer. By using the results generated by multiple tones, it is possible to triangulate the ΔL by sweeping the potential n values and seeking a global solution that satisfies the phase results of all $\Delta\omega_{i,j}$.

Moreover, the unambiguous range (L_u) is a well-known parameter in lidars that refers to the maximum range a target can be located with the known system parameters such as pulse repetition rate or frequency sweep period [41]. For CLAN, L_u corresponds to the furthest distance of the target receiver, while $n = 1$ for the lowest frequency. The repetitive nature of the phase will yield $L_u = c/f_{gcd}$, where f_{gcd} is the greatest common divisor of the selected f_i or the reference clock frequency of the synchronized RF synthesizers. Mixing the RF tones with a low-frequency modulation paves the way to enhance the range of the system by lowering the f_{gcd} to kHz levels. In such a configuration, where one of the tones is RF mixed with a kHz level f_{low}, the unambiguous range will be determined by the f_{low}, and the new L_u will be defined as $L_u = c/2f_{low}$. Here, up and down-shifted mixed frequencies ($f_i \pm f_{low}$) are evaluated separately by filtering and RF mixing $f_i + f_{low}$ with f_i - f_{low} to acquire the coarse range information using (5). Then, the fine ranging is performed using all the $\omega_t - \omega_r + \omega_i$ or $\omega_t - \omega_r - \omega_i$ depending on the availability of the bandwidth.

$$\Delta L = \frac{(2\pi n + \Delta\phi_{i,j})\, c}{\Delta\omega_{i,j}} \tag{5}$$

In the case of a dynamic target, the optical carrier and the sidebands will realize a Doppler frequency shift proportional to the target's velocity in the direction of beam propagation. The Doppler shift on the carrier will manifest itself as an additional frequency shift to the resultant spectrum. Hence, the expected photocurrent, I_{pd}, with Doppler shift, $\omega_d = (2v/c) \times \omega_t$ [42], is given in (6). Here, v is the target's velocity and ω_d^i is the Doppler shift realized by the tone frequency, ω_i. Since tone frequencies are much smaller than the carrier frequencies, $\omega_i << \omega_0$, the relative Doppler shift between tones is negligible. Therefore, we assume all tones have the same Doppler shift and define the resultant I_{pd} spectrum with a $\pm f_d$ ($\omega_d = 2\pi f_d$) frequency shift. However, after RF mixing the I_{pd} with the isolated $f_t - f_r \pm f_d$ peak, the spectrum will down-shift back to the baseband. Moreover, since the frequency resolution is limited by the time window, a record length of 1 ms leads to about 1 kHz frequency resolution. In such record lengths, it is challenging to extract the relative Doppler shifts between different tones in the CLAN configuration. Therefore, the velocity of the target Rx can be computed by comparing the displacement between multiple frames using $v = dx/dt$. However, increasing the record length may allow the detection of relative Doppler shifts between tones and single-shot velocity measurements.

To verify the CLAN concept and give a clear explanation of the triangulation algorithm as well as to assess the system performance and validity of the experimental results, we have conducted a series of numerical simulations. Firstly, the behavior of the modulated light is transferred to the software domain by using (1) and (2). Then, the time window is set to 1024 μs with 2^{22} samples per run, yielding a time resolution of 244 ps. The time domain values translate to the frequency domain as 2 GHz bandwidth and ~1 kHz frequency resolution. The system's central wavelength is 1064 nm, and the lasers used as Tx and Rx were set to have a randomly selected arbitrary frequency difference of 677 MHz, which is within the detection bandwidth. The laser output is modulated on the Tx side by an MZM with m = 0.01. 4 RF modulation frequencies are selected to be 500, 700, 890, and 950 MHz (matching the experiment) and are phase-locked to modulate the optical carrier. The considerations behind selecting RF tones are to prevent the anticipated cross-beatings and second harmonics. Furthermore, an additional 500 kHz (as in the experiment) is employed as a low-frequency component to achieve coarse ranging. This f_{low} is RF-mixed with the 500 MHz tone to realize a subcarrier modulation. The received signal is then coupled with the modulation-free Rx laser and converted to the photocurrent I_{pd} at the photodetector. Noise components of the detector including shot noise, thermal noise, and dark current are omitted for simplicity. The subcarrier modulation with the low-frequency signal results in an unambiguous range of 300

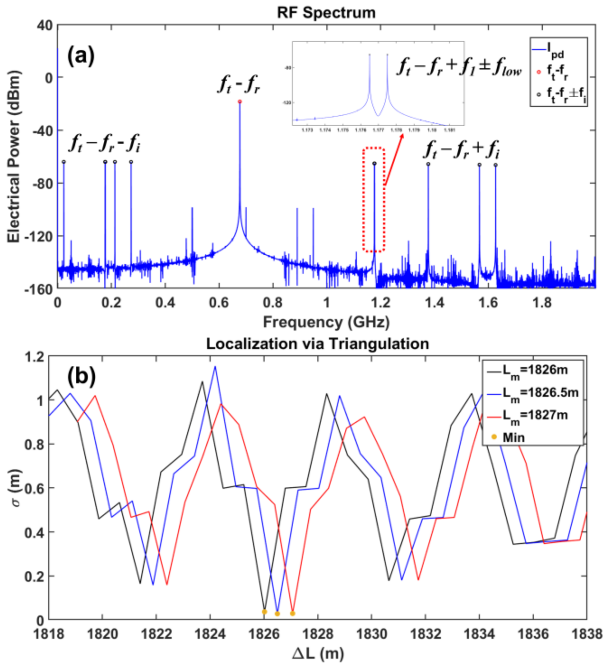

Fig. 3. Simulation results. (a) The resultant photocurrent spectrum. The subcarrier modulation is indicated in the inset for coarse ranging. (b) The result of the triangulation algorithm for three consecutive distances.

m and the number of cycles is set to six to match the target range for a target at >1.8 km distance. Based on the simulation parameters, the Rx is distanced from the Tx at three arbitrarily chosen in-range locations with a 50 cm of increment, which are 1826 m, 1826.5 m, and 1827 m, respectively.

$$I_{pd} = I_{DC} + A' \cos((\omega_t - \omega_r \pm \omega_d)t + \omega_t \frac{\Delta L}{c} + \Phi + \phi_n^t(t-\tau) - \phi_n^r(t)) - A'' \left[\sum_{i=1}^{N} \cos \begin{pmatrix} (\omega_t - \omega_r \pm \omega_d + \omega_i \pm \omega_d^i)\, t + (\omega_t + \omega_i)\, \frac{\Delta L}{c} \\ + \Phi + \phi_i^{RF} + \phi_n^t(t-\tau) - \phi_n^r(t) \end{pmatrix} + \sum_{i=1}^{N} \cos \begin{pmatrix} (\omega_t - \omega_r \pm \omega_d - \omega_i \pm \omega_d^i)\, t - (\omega_t - \omega_i)\, \frac{\Delta L}{c} \\ + \Phi - \phi_i^{RF} - \phi_n^t(t-\tau) - \phi_n^r(t) \end{pmatrix} \right] \quad (6)$$

Fig. 3(a) demonstrates the I_{pd} spectrum with the indicated frequencies. The highest power peak is attributed to the frequency difference between Rx and Tx lasers, which is 677 MHz as expected. In the inset, the subcarrier modulation on the 500 MHz tone (f_1) with the f_{low} is indicated and the frequency difference between $f_t - f_r + f_1 \pm f_{low}$ is found as 1MHz. These two terms are filtered and the phase and frequency information of the subcarriers are used as in (5) to compute the coarse range by setting $n = 6$ (as in the experiment). Then, within a $\pm$15 m range around the coarse position, possible integer values of n are calculated for each IF term using the known frequencies of preselected RF sidebands. After determining the potential n values, (5) is employed and all solutions of ΔL are computed for all IF values within the predefined ranges of the corresponding n. For each $\Delta\omega_{i,j}$, the results are stored inside the corresponding column of a data matrix, and the standard deviation of each row of the calculated potential distances is computed by the algorithm. As a result, the mean value of the row with the lowest standard deviation indicates the measured ΔL. In other words, the solutions of (5) for each $\Delta\omega_{i,j}$ for different n values should converge to the same ΔL, which corresponds to the output with the lowest standard deviation. The details about the triangulation process and the complete methodology can be found in [36], [37]. The results of the triangulation operation for three consecutive Rx positions are displayed in Fig. 3(b). The points at which the minimum standard deviations are marked with yellow circles. The corresponding L values are 1826.0 m, 1826.5 m, and 1827 m, respectively.

Moreover, the phase resolution of the system, which is determined by the time resolution (dt), defines the measurement resolution (δL). Here, dt is 244 ps and based on $\delta L = c \times dt$, the minimum theoretical resolution the CLAN approach provides is 7.3 cm for this simulation. By performing a Spline interpolation, it is possible to further enhance the resolution of the system [43]. The accuracy of the measurements on the other hand depends on additional factors such as sampling rate, jitter, total noises in the system, etc. Furthermore, the precision of the CLAN is determined by the SNR of the system architecture which is directly related to the detection electronics [36], [41].

IV. Experimental Verification

Fig. 4 illustrates the experimental setup to test the capabilities of the CLAN. Tx and Rx lasers used in the system have <100 kHz linewidth (RPMC Lasers). The central wavelengths are delicately adjusted by fine-tuning the operating temperature of both lasers to have a frequency difference of <2 GHz to stay within the bandwidth of detection electronics. The Tx laser operates at 30.7 mW, while the Rx side output power is set to 21.76 mW. An MZM (iXblue) with 10GHz modulation bandwidth and 30 dB extinction ratio is placed after the Tx laser and biased at the quadrature point. 4-phase locked RF frequencies which are generated by phase-locked RF synthesizers (Windfreak Technologies) at 500, 700, 890, and 950 MHz with the same 10 MHz reference clock utilized for modulation. The modulation depth is <0.1 based on the RF voltage values. To perform the coarse ranging, an additional 500 kHz low-frequency signal is also RF mixed with the 500 MHz tone. A subharmonic of the 10 MHz reference clock is also employed to phase-lock the low-frequency component with the main tones. To mimic the free space propagation of light in long distances and to test the system's capability at long ranges, a ~1.2 km long fiber spool (HI-1060) corresponds to about 1.8 km optical path length in free space, is introduced to the system. A motorized translational stage controls the positioning of the target. The target reflector is moved to four different locations with a 10 cm separation and at each location 10 measurements are performed for static target ranging. The collection of the echo signal from the reflector is achieved by using a beam splitter (BS) placed in the optical path. After the BS, returning signal is transmitted to the Rx collimator (CL), which further couples into a fiber. It is important to note that the fiber coupling is an experiment-specific operation for the introduced all-fiber system. For more complicated systems,

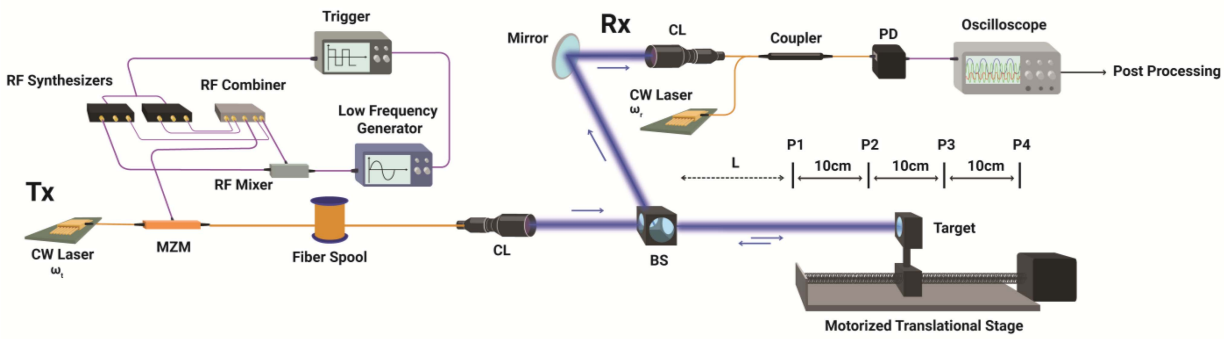

Fig. 4. Experimental setup for proof-of-concept experiments to test the CLAN technique.

it can be done in free space as was previously demonstrated for a CubeSat system [44]. Finally, the signal interferes with the free-running Rx laser via a fiber coupler. The resultant interference signal is fed to a balanced photodetector (BPD) (Thorlabs PDB-482C-AC) with ∼2.5 GHz bandwidth.

A digital storage oscilloscope (Tektronix – TDS7704B) which has a 7 GHz bandwidth with a 20 GSa/s sampling rate is used for data collection. The time window of the measurements is set to 100 μs and the time resolution is selected as 100 ps corresponding to a 5 GHz measurement bandwidth with a 10 kHz frequency resolution. Initially, data is interpolated to achieve a higher time resolution of 23.8 ps. In addition, to impede any potential distortions caused by the residual RF phases due to the synthesizers and optical path to the Tx CL, Tx is calibrated prior to the measurements.

The spectrum of the raw I_{pd} data for the measurement, while the target is at P_1, is presented in Fig. 5(a). Here, the f_t - f_r peak is indicated with the red dot on the spectrum and it corresponds to 593 MHz. Hence, the modulation sidebands are shifted as much as f_t - f_r. A 20 MHz Butterworth bandpass filter center at 593 MHz is utilized to isolate the $f_t - f_r$ peak. Using this peak and the apriori-knowledge of the static tone frequencies, the tones are located on the RF spectrum and marked as black dots on the spectrum. The 700 MHz tone is portrayed in the inset of Fig. 5(a). This tone is shifted to ∼1293 MHz and accumulates the phase noise generated by both Tx and Rx lasers. To eliminate the common noise terms on the sidebands, the entire spectrum is RF mixed with the filtered $f_t - f_r$ peak (red dot). The resultant IF spectrum is depicted in Fig. 5(b), in which the sidebands shift back to the baseband. Hence, the corresponding peaks are now stationed at their original preset frequencies. The 700 MHz tone after RF mixing is given in the inset of Fig. 5(b). When both insets of Fig. 5 are compared, it is evident that the phase noise induced by the Tx and Rx lasers diminishes after RF mixing of the I_{pd} with filtered $f_t - f_r$ signal. The phase-noise-free RF tones possess the distance information in their phases to be used in triangulation algorithms.

The measurements are performed for 4 positions, P_1, P_2, P_3, and P_4. Each position has a ∼10 cm separation, and 10 measurements are performed at each location. The 10 cm displacement corresponds to a ∼20 cm light propagation considering the roundtrip from the target to the BS. The actual optical propagation is ∼1800 m due to the ∼1.2 km fiber. To understand the

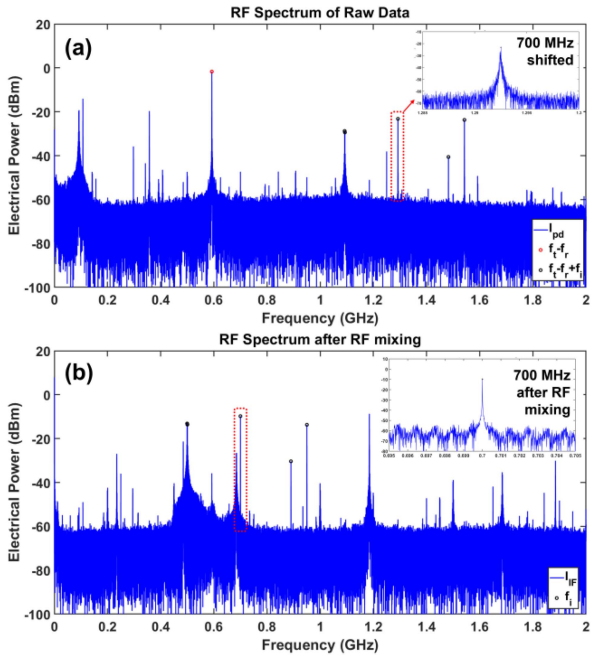

Fig. 5. (a) RF spectrum of the raw data. The inset shows the shifted 700 MHz tone at 1293 MHz after Tx and Rx beating. (b) RF spectrum of the IF signal after RF mixing the data with the laser peak. Inset represents the phase noise-free 700 MHz tone at the baseband after RF mixing.

actual path traveled by the light, we employed a 5 ns pulse with a 10 kHz repetition rate to perform a pulsed time-of-flight (ToF) measurement. The laser source is split into two, one branch is used as a reference, and the other is connected to the MZM as in Fig. 4 to compute the ToF. The average of 15 pulse measurements yields 1826.35 ± 0.15 m of total propagation distance.

We used the ±500 kHz subcarrier modulation on the 500 MHz RF tone to compute the coarse ranging. As discussed earlier, the unambiguous range corresponds to ∼300 m. Since $\Delta L > L_u$ we considered a priori knowledge of the target's whereabouts, meaning that the signal will complete 6 full cycles ($n = 6$) for the low-frequency components. The coarse ranging narrows the target position to a 30 m range ($f_{gcd} = 10$ MHz) to be estimated with the high-frequency sidebands. As a result, the subcarrier modulation indicated a position between 1810–1840 m. It is possible to further improve the L_u by introducing lower frequency

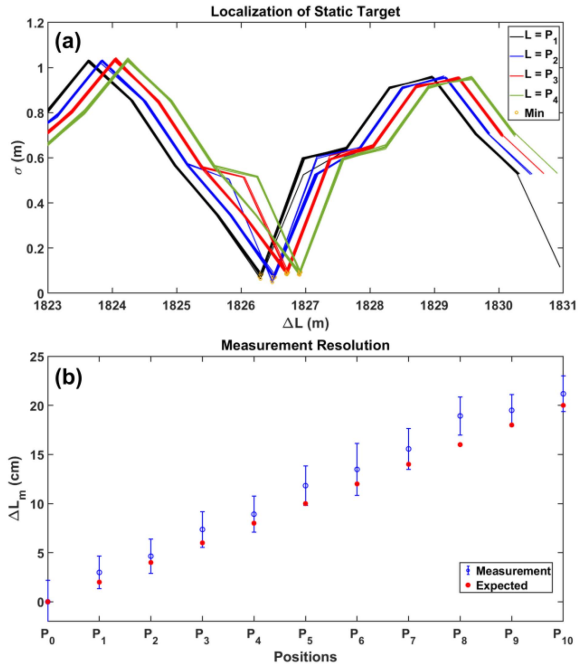

Fig. 6. (a) Triangulation results of the proof-of-concept experiments for 10 trials at 4 different positions separated by 10 cm displacements at ∼1.8 km distance. (b) High-resolution measurement results with the target being separated by 1 cm displacements at ∼1.8 km distance.

terms and increasing the time window of the measurement based on the target application ranges.

The complete position triangulation results for 10 trials at each position are presented in Fig. 6(a). Here, black, blue, red, and green colors correspond to P_1, P_2, P_3, and P_4. The minimum standard deviation points indicated with yellow circles correspond to the measured ΔL of a given trial. The average measured distances are 1826.30 m, 1826.50 m, 1826.71 m, and 1827.91 m, respectively. Similarly, the displacement between each position is measured as 20.3 cm, 21.1 cm, and 19.4 cm, respectively. The errors in the displacement can be attributed to potential thermal variations in the long fiber spool and human error during the target placement. Moreover, the precision of the localization is found by calculating the standard deviation of 10 trials at each position. The measured precisions are 1.1 cm, 1.3 cm, 1.5 cm, and 0.9 cm, respectively, at a distance of $>$1.8 km. The system's precision depends on the SNR, and the SNR depends not only on the bandwidth of the detection electronics but also on many factors that vary with the system design and application purposes such as wavefront distortion, divergence angle, aberrations, etc. For this reason, these potential variations are left out of the SNR analysis and the received optical power is kept as the only determining factor. In this proof-of-concept experiment, the coupled Tx signal power before the detector is $<$10 μW for the trials. It is also possible to utilize narrow bandpass filters around the tones to further enhance the SNR of the system [36]. The phase prediction is determined by the SNR and the number of cycles captured in a single time window. Based on our numerical analysis, we observe that the phase prediction works accurately if the SNR$>$10 dB. The

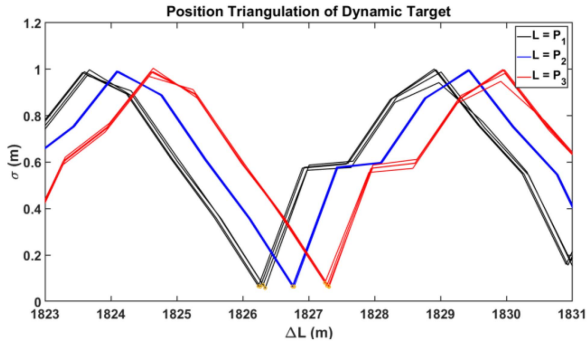

Fig. 7. Dynamic target localization at three positions.

positioning resolution δL depends on the phase resolution of the system, which also depends on the time resolution (dt) as$\delta L \sim d\phi_i \times c/\omega_i = dt \times c$. Here, the dt is reduced by data interpolation to 23.8 ps, which yields a $<$1 cm theoretical δL. To test this, the target moved with 1 cm increments on the stage, which corresponds to a total of 2 cm displacement between each position at ∼1.8 km. The results are presented in Fig. 6(b), where P_0 is the first position, and all other positions are referenced to P_0 with 2 cm displacements consecutively. The error bars represent the standard deviation of 10 measurements at each step, and expected displacements are represented with red dots. The measured distances are within the measurement precision range, indicating CLAN's high-resolution localization capability over long distances. Therefore, CLAN has the capability to resolve $<$2 cm displacements at a range of ∼2 km. The time-based systems such as GPS and cooperative localization also provide reliable navigation and localization information. However, a timing error might result in large-ranging errors. The clock-independent CLAN is mainly limited by the SNR of the system. Hence, the desired architecture can be utilized based on the requirements and specifications of the system.

As the last proof-of-concept experiment, we performed localization of a dynamic target with the CLAN. The motorized stage is set to operate at the maximum speed of ∼21 cm/s, which is also measured with the photonic Doppler velocimetry technique [42], and a Doppler shift of 393.3±32 kHz is measured over 20 trials. Three P_1, P_2, and P_3 locations are selected with 20 cm consecutive displacements corresponding to a ∼40 cm light propagation difference. The data is captured with a manual trigger while the target is passing the predetermined locations. For convenience, 10 trials are performed at each position, and 4 results are displayed in Fig. 7. The mean of the measurements is 1826.29 m, 1826.76 m, and 1827.28 m, respectively. The precisions are computed as 3.2 cm, 2.1 cm, and 2.5 cm, respectively, which are attributed to the manual trigger that causes minor position variations. As a result, it is possible to locate a dynamic Rx with respect to a Tx using the CLAN technique. At the same time, the comparison of multiple frames with a certain frame rate can also yield the velocity of the target.

V. Conclusion

In this article, we demonstrate the capabilities of clock-free photonics positioning and localization, namely CLAN. The Tx and Rx have separate free-running lasers to enhance the SNR by employing optical heterodyne detection. Phase and frequency information of multiple preselected phase-locked RF tones on the optical carrier is employed for Rx localization. We demonstrate the CLAN's concept, theoretical background, and working principle. Moreover, we performed proof-of-concept experiments over a >1.8 km optical path length and showed <2 cm localization precision. Furthermore, we demonstrated the high-resolution capability of CLAN by resolving 2 cm increments over a 1.8 km optical path. Finally, we performed positioning of a dynamic target with respect to Tx and showed that it is possible to perform velocimetry along with the localization of a given target. Results indicate that the CLAN has the potential to pave the way for high-resolution and high-precision photonic localization and navigation, where conventional navigation methods are limited, restricted, or denied.

References

[1] G. Mintsis et al., "Applications of GPS technology in the land transportation system," *Eur. J. Oper. Res.*, vol. 152, pp. 399–409, 2004.

[2] R. B. Langley, "Propagation of the GPS signals," in *GPS for Geodesy*, A. Kleusberg and P. J. G. Teunissen, Eds. Berlin, Germany: Springer, 1996, pp. 103–140.

[3] H. B. Baby et al., "A model for the tropospheric excess path length of radio waves from surface meteorological measurements," *Radio Sci.*, vol. 23, pp. 1023–1038, 1988.

[4] A. Amini, R. M. Vaghefi, J. M. de la Garza, and R. M. Buehrer, "Improving GPS-based vehicle positioning for intelligent transportation systems," in *Proc. IEEE Intell. Veh. Symp.*, 2014, pp. 1023–1029.

[5] Y. Zein et al., "GPS tracking system for autonomous vehicles," *Alexandria Eng. J.*, vol. 57, no. 4, pp. 3127–3137, 2018.

[6] W. Featherstone, "The global positioning system (GPS) and its use in geophysical exploration," *Explor. Geophys.*, vol. 26, pp. 1–18, 1995.

[7] F. Van Diggelen and C. Abraham, *Indoor GPS Technology*, Washington, DC, USA: CTIA Wireless-Agenda, vol. 89, 2001.

[8] M. R. Yousefi and A. M. Razdari, "Application of GIS and GPS in precision agriculture (a review)," *Int. J. Adv. Biol. Biomed. Res.*, vol. 3, no. 1, pp. 7–9, 2015.

[9] S. Kumar and K. B. Moore, "The evolution of global positioning system (GPS) technology," *J. Sci. Educ. Technol.*, vol. 11, pp. 59–80, 2002.

[10] Q. D. Hua, M. S. Williams, J. Evans, and M. A. Trippy, "Use of the NAVSTAR global positioning system (GPS) in the defense communications system (DCS)," in *Proc. IEEE Int. Freq. Control Symp.*, 1993, pp. 40–44.

[11] B. Hofmann-Wellenhof, H. Lichtenegger, and J. Collins, *Global Positioning System: Theory and Practice*. Berlin, Germany: Springer, 2012.

[12] P. K. Enge, "The global positioning system: Signals, measurements, and performance," *Int. J. Wireless Inf. Netw.*, vol. 1, no. 2, pp. 83–105, 1994.

[13] G. Xu and Y. Xu, *GPS: Theory, Algorithms and Applications*. Berlin, Germany: Springer, 2016.

[14] Y. Bock and D. Melgar, "Physical applications of GPS geodesy: A review," *Rep. Prog. Phys.*, vol. 79, no. 10, 2016, Art. no. 106801.

[15] J. McEllroy, "Navigation using signals of opportunity in the AM transmission band," M.S. thesis, Dept. Elect. Comput. Eng., Air Force Inst. Technol., Wright-Patterson AFB, OH, USA, 2006.

[16] J. F. Raquet et al., "Issues and approaches for navigation using signals of opportunity," in *Proc. Nat. Tech. Meeting Inst. Navigation*, 2007, pp. 1073–1080.

[17] M. Robinson and R. Ghrist, "Topological localization via signals of opportunity," *IEEE Trans. Signal Process.*, vol. 60, no. 5, pp. 2362–2373, May 2012.

[18] V. Moghtadaiee, A. G. Dempster, and S. Lim, "Indoor localization using FM radio signals: A fingerprinting approach," in *Proc. Int. Conf. Indoor Positioning Indoor Navigation*, 2011, pp. 1–7.

[19] Y. Zhang and K. C. Ho, "Localization by signals of opportunity in the absence of transmitter position," *IEEE Trans. Signal Process.*, vol. 70, pp. 4602–4617, 2022.

[20] R. Lutwak, "Micro-technology for positioning, navigation, and timing towards PNT everywhere and always," in *Proc. Int. Symp. Inertial Sensors Syst.*, 2014, pp. 1–4.

[21] F. R. Giorgetta et al., "Optical two-way time and frequency transfer over free space," *Nature Photon.*, vol. 7, no. 6, pp. 434–438, 2013.

[22] M. Maheepala, A. Z. Kouzani, and M. A. Joordens, "Light-based indoor positioning systems: A review," *IEEE Sensors J.*, vol. 20, no. 8, pp. 3971–3995, Apr. 2020.

[23] Z. Li, A. Yang, H. Lv, L. Feng, and W. Song, "Fusion of visible light indoor positioning and inertial navigation based on particle filter," *IEEE Photon. J*, vol. 9, no. 5, Oct. 2017, Art. no. 7906613.

[24] F. Zhang et al., "Photonics-based MIMO radar with high-resolution and fast detection capability," *Opt. Exp.*, vol. 26, no. 13, pp. 17529–17540, Jun. 2018.

[25] S. Hrabar and G. Sukhatme, "Vision-based navigation through urban canyons," *J. Field Robot.*, vol. 26, no. 5, pp. 431–452, 2009.

[26] S. Hrabar, G. S. Sukhatme, P. Corke, K. Usher, and J. Roberts, "Combined optic-flow and stereo-based navigation of urban canyons for a UAV," in *Proc. IEEE/RSJ Int. Conf. Intell. Robots Syst.*, 2005, pp. 3309–3316.

[27] J. A. Christian, "StarNAV: Autonomous optical navigation of a spacecraft by the relativistic perturbation of starlight," *Sensors*, vol. 19, no. 19, 2019, Art. no. 4064.

[28] J. Rebordão, "Space optical navigation techniques: An overview," in *Proc. 8th Iberoamerican Opt. Meeting 11th Latin Amer. Meeting Opt., Lasers, Appl.*, 2013, vol. 8785, pp. 29–48.

[29] E. Turan et al., "Autonomous navigation for deep space small satellites: Scientific and technological advances," *Acta Astronautica*, vol. 193, pp. 56–74, Apr. 2022.

[30] R. Mautz and S. Tilch, "Survey of optical indoor positioning systems," in *Proc. Int. Conf. Indoor Positioning Indoor Navigation*, 2011, pp. 1–7.

[31] W. M. Owen, "Methods of optical navigation," Jet Propulsion Lab., Pasadena, CA, USA, Tech. Rep. AAS 11-215, 2011.

[32] Y. L. Li, "Photonic systems engineering: A structured approach to positioning, navigation and timing using microresonators," in *Proc. Conf. Lasers Electro-Opt.*, 2021, pp. 1–2.

[33] D. J. Blumenthal, "Integrated ultra-narrow linewidth ultra-stable brillouin lasers and their application to PNT applications," in *Proc. Conf. Laser Electro-Opt.*, 2021, pp. JTu1I–JTu13.

[34] S. Huang and R. Tjoelker, "Stabilized photonic links for deep space tracking, navigation, and radio science applications," in *Proc. 43rd Annu. Precise Time Time Interval Syst. Appl. Meeting*, 2011, pp. 1–8.

[35] M. Calhoun, S. Huang, and R. L. Tjoelker, "Stable photonic links for frequency and time transfer in the deep-space network and antenna arrays," *Proc. IEEE*, vol. 95, no. 10, pp. 1931–1946, Oct. 2007.

[36] M. M. Bayer et al., "Single-shot ranging and velocimetry with a CW lidar far beyond the coherence length of the CW laser," *Opt. Exp.*, vol. 29, no. 26, pp. 42343–42354, Dec. 2021.

[37] M. M. Bayer and O. Boyraz, "Ranging and velocimetry measurements by phase-based MTCW LiDAR," *Opt. Exp.*, vol. 29, no. 9, pp. 13552–13562, Apr. 2021.

[38] S. S. Kia, S. Rounds, and S. Martinez, "Cooperative localization for mobile agents: A recursive decentralized algorithm based on Kalman-filter decoupling," *IEEE Control Syst. Mag.*, vol. 36, no. 2, pp. 86–101, Apr. 2016.

[39] M. M. Bayer et al., "Photonics PNT based on multi-tone continuous wave ranging," in *Proc. Conf. Lasers Electro-Opt.: Sci. Innovations*, 2022, pp. JTh3A–JTh57.

[40] M. M. Bayer et al., "Enhancing the multi-tone continuous-wave lidar with phase detection," in *Proc. Soc. Photographic Instrum. Eng.-Open Data Sci. Conf. Ind. Opt. Devices Syst.*, 2021, vol. 11828, pp. 24–31.

[41] P. F. McManamon, *LiDAR Technologies and Systems*. Bellingham, WA, USA: SPIE, 2019.

[42] D. H. Dolan, "Accuracy and precision in photonic Doppler velocimetry," *Rev. Sci. Instrum.*, vol. 81, no. 5, 2010, Art. no. 053905.

[43] G. Wahba, "Spline interpolation and smoothing on the sphere," *Soc. Ind. Appl. Math. J. Sci. Stat. Comput.*, vol. 2, no. 1, pp. 5–16, 1981.

[44] G. Guentchev et al., "Mechanical design and thermal analysis of a 12U CubeSat MTCW lidar based optical measurement system for littoral ocean dynamics," *Proc. SPIE*, vol. 11832, pp. 71–98, 2021.